Spontaneous neurotransmission at evocable synapses predicts their responsiveness to action potentials

Andreas T. Grasskamp[1], Meida Jusyte[1,2], Anthony W. McCarthy[1], Torsten W.B. Götz[1], Susanne Ditlevsen[3], Alexander M. Walter[1,2,4,*]

[1]Leibniz-Forschungsinstitut für Molekulare Pharmakologie, Berlin, Germany

[2]Einstein Center for Neurosciences, Charité Universitätsmedizin Berlin, Berlin, Germany

[3]Department of Mathematical Sciences, University of Copenhagen, Copenhagen, Denmark

[4]Department of Neuroscience, University of Copenhagen, Copenhagen, Denmark

*Corresponding author: awalter@sund.ku.dk

Department of Neuroscience, University of Copenhagen, Denmark

ORCID: 0000-0002-5895-6529 (A.T.G.), 0000-0001-9948-871X (M.J.), 0000-0002-3771-351X (A.W.M.), 0000-0002-1998-2783 (SD), 0000-0001-5646-4750 (A.M.W.)

Abstract

Synaptic transmission relies on presynaptic neurotransmitter (NT) release from synaptic vesicles (SVs) and on NT detection by postsynaptic receptors. Transmission exists in two principal modes: action-potential (AP) evoked and AP-independent, "spontaneous" transmission. AP-evoked neurotransmission is considered the primary mode of inter-neural communication, whereas spontaneous transmission is required for neuronal development, homeostasis, and plasticity. While some synapses appear dedicated to spontaneous transmission only, all AP-responsive synapses also engage spontaneously, but whether this encodes functional information regarding their excitability is unknown. Here we report on functional interdependence of both transmission modes at individual synaptic contacts of *Drosophila* larval neuromuscular junctions (NMJs) which were identified by the presynaptic scaffolding protein Bruchpilot (BRP). Consistent with its role in organizing the AP-dependent release machinery (voltage-dependent Ca^{2+} channels and SV fusion machinery), most active BRP-positive synapses (>85%) responded to APs. At these synapses, the level of spontaneous activity was a precise predictor for their responsiveness to AP-stimulation. Both transmission modes engaged an overlapping pool of SVs and NT-receptors, and both were affected by the non-specific Ca^{2+} channel blocker cadmium. Thus, by using overlapping machinery, spontaneous transmission is a continuous, stimulus independent predictor for the AP-responsiveness of individual synapses.

33 ## Introduction

34 Synaptic transmission relies on quantal neurotransmitter (NT) release from synaptic vesicles
35 (SVs) fusing with the plasma membrane at presynaptic active zones (AZs) and on subsequent NT
36 detection by postsynaptic receptors (Südhof, 2013). Transmission is evoked by action-potentials
37 (APs) but can also occur "spontaneously" in the absence of a stimulus (Fatt and Katz, 1952;
38 Kaeser and Regehr, 2014; Schneggenburger and Rosenmund, 2015).

39 In evoked transmission, APs depolarize the membrane potential, inducing voltage-gated Ca^{2+}
40 channel opening and Ca^{2+}-influx. Subsequently, Ca^{2+} binds to an SV-associated Ca^{2+} sensor
41 (synaptotagmin-1 or -2) and induces SV fusion (Littleton and Bellen, 1995; Kochubey et al.,
42 2011; Südhof, 2012a) which depends on the formation of the neuronal SNARE complex
43 consisting of vesicular VAMP2/Synaptobrevin and the plasma membrane proteins SNAP-25 and
44 syntaxin-1 (Südhof and Rothman, 2009; Jahn and Fasshauer, 2012; Rizo, 2018). AP-evoked NT
45 release further requires the SNARE-binding proteins (M)Unc13 and (M)Unc18 (Brose et al.,
46 2000; Richmond and Broadie, 2002; Toonen and Verhage, 2007; Dittman, 2019). Additionally,
47 AZ cytomatrix proteins like Rab3-interacting molecule (RIM), RIM-binding protein (RBP), and
48 ELKS/Bruchpilot (BRP) contribute to AP-evoked transmission by organizing this release
49 machinery (Südhof, 2012b; Held and Kaeser, 2018; Walter et al., 2018).

50 In various synapses and model systems, spontaneous transmission was shown to utilize SVs, NT
51 receptors, Ca^{2+} sensors and SNARE proteins separate from ones used during AP-evoked
52 transmission (Broadie et al., 1995; Deitcher et al., 1998; Koenig and Ikeda, 1999; Schoch et al.,
53 2001; Sara et al., 2005; Atasoy et al., 2008; Fredj and Burrone, 2009; Groffen et al., 2010; Sara
54 et al., 2011; Ramirez et al., 2012; Bal et al., 2013; Peled et al., 2014; Courtney et al., 2018). Live

55 imaging experiments furthermore revealed spatial segregation of both transmission modes with
56 no or negative correlation between them (Melom et al., 2013; Peled et al., 2014; Reese and
57 Kavalali, 2016; Farsi et al., 2021). Accordingly, spontaneous transmission was suggested to form
58 a communication channel distinct from AP-evoked activity which may fulfil essential roles in
59 synapse development (Kavalali, 2015). However, at the same time, spontaneous transmission
60 also occurs at all AP-evocable synapses where the same pool of SVs was implicated to cycle
61 spontaneously and during AP-stimulation (Groemer and Klingauf, 2007; Hua et al., 2010;
62 Wilhelm et al., 2010). To what extend spontaneous signals in this "mixed channel" carry
63 information of physiological relevance is unknown.

64 To investigate this "mixed channel" we here focused on the analysis of spontaneous transmission
65 at AP-responsive AZs of the *Drosophila* neuromuscular junction (NMJ) identified by the
66 scaffolding protein BRP. We show that at these AZs, AP-evoked and spontaneous transmission
67 are highly inter-dependent, and the spontaneous activity predicts AP-responsiveness. Both
68 transmission modes depend on an overlapping machinery on both pre- and postsynaptic sides.
69 Based on these data, we propose that spontaneous activity at AP-evocable synapses serves as a
70 scalable, highly uniform readout of connectivity strength likely relevant for synapse maintenance
71 and plasticity.

72 **Results**

73 One of the difficulties in assessing the relation between spontaneous and AP-evoked
74 transmission has been the inability to simultaneously monitor both activity modes at the level of
75 individual synaptic connections. This was improved by the development of elegant live-imaging
76 approaches to track synaptic activity with high spatial resolution (Peled and Isacoff, 2011;
77 Melom et al., 2013; Peled et al., 2014; Reese and Kavalali, 2016; Tang et al., 2016; Sakamoto et
78 al., 2018; Farsi et al., 2021). We here use such an assay to monitor synaptic activity at the
79 *Drosophila* 3rd instar larval NMJs (type Ib boutons of muscle 4). In this assay, we
80 postsynaptically express the fluorescent Ca^{2+}-reporter GCaMP5 which reports on changes in
81 Ca^{2+}-levels induced during synaptic transmission due to the Ca^{2+} permeability of open
82 postsynaptic glutamate receptors (Melom et al., 2013; Reddy-Alla et al., 2017) (**Figure 1A,B**).
83 We confirmed that such fluorescent signals reliably report on synaptic activity in combined
84 electrophysiological experiments (**Figure 1 - figure supplement 1A-F**).

85 We wanted to track transmission at AP-responsive synapses and therefore restricted our analysis
86 to AZs containing the cytomatrix protein BRP which organizes the AP-sensitive release
87 machinery (e.g. voltage gated Ca^{2+} channels and Unc13A release sites (Kittel et al., 2006;
88 Fouquet et al., 2009; Böhme et al., 2016)). To do so, GCaMP movies of live activity were
89 aligned to confocal images obtained post-hoc of the same NMJs stained against BPR (see
90 methods for details) (**Figure 1C,D**). The local temporal GCaMP fluorescence profiles were then
91 read out at equally sized regions of interest (ROIs) placed on all BRP-positive synaptic contacts
92 (**Figure 1E**). Even though postsynaptic Ca^{2+} dispersion caused elevated GCaMP signals at
93 multiple ROIs in response to single events, the signal intensity steeply decreased from the origin
94 to the periphery, allowing signal assignment (highest peak) of temporally scattered spontaneous

events to one AZ (**Figure 1E**). Additionally, for AP-evoked responses a distance threshold (2.5 µm) between locations was imposed to prevent that the same event was counted more than once. In principle this could cause a slight under-estimation of AP-evoked activity, but such cases are rare, due to the overall low activity of individual AZs (Muhammad et al., 2015). We first assessed spontaneous activity by imaging signals for 100 s without stimulation. The AP-evoked activity of the same AZs was assessed afterwards in a separate recording where 36 AP stimuli were administered at a frequency of 0.2 Hz (**Figure 1E,F** and **Figure 1 – figure supplement 1G**). The time course and amplitude of NT-induced GCaMP signals were indistinguishable for spontaneous- and AP-evoked release (**Figure 1F**) and GCaMP amplitudes were non-saturating at a Ca^{2+} concentration of 1.5 mM in the external medium ($[Ca^{2+}]_{ext}$) (**Figure 1 – figure supplement 1H**), confirming the quantal resolution of this assay (see methods and **Figure 1 – figure supplement 1&-2**).

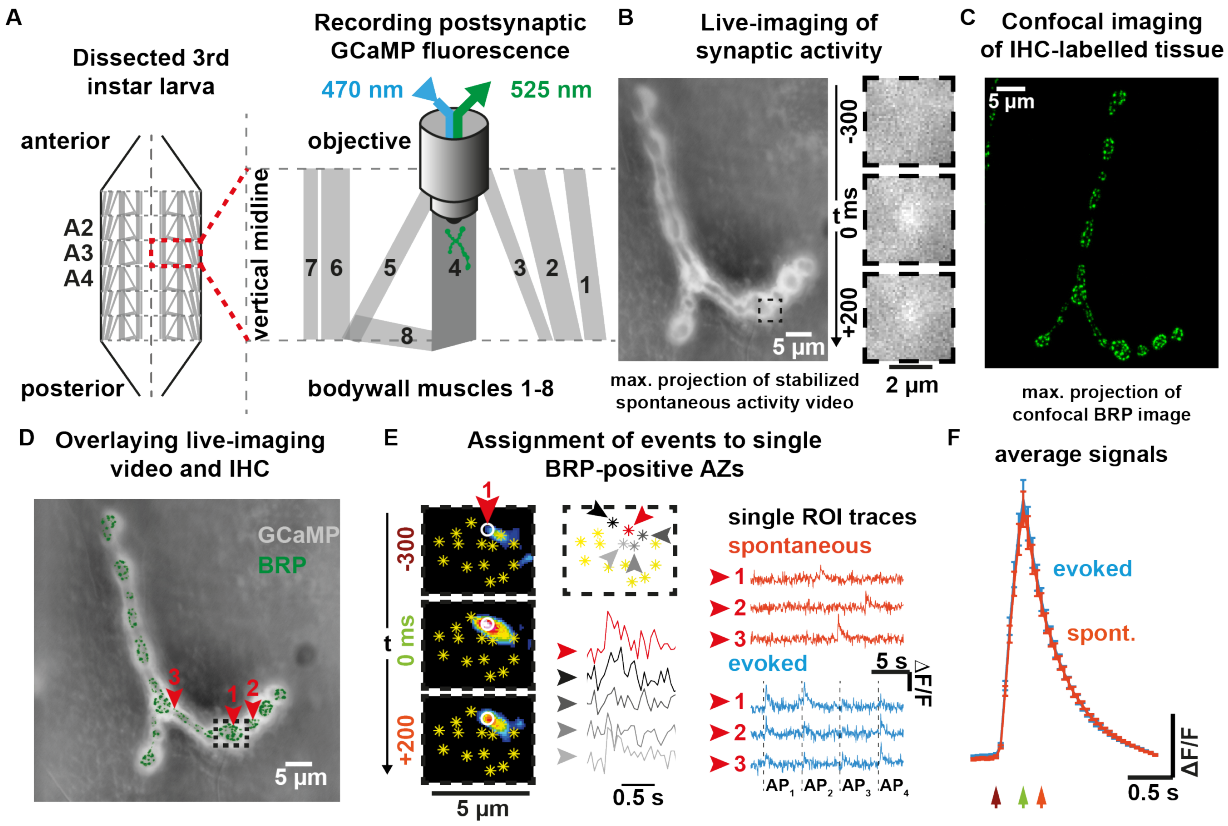

Figure 1. Postsynaptic fluorescence measurements of presynaptic activity with single AZ precision. (**A**) Scheme of experiment to measure Ca^{2+} induced fluorescence signals in *Drosophila* larvae postsynaptically expressing GCaMP. (**B**) Left: Contrast adjusted maximal projection of stabilized 100 s spontaneous activity video; Right: 500 ms time sequence of single event observed in indicated sub-frame. (**C**) Confocal image obtained after immunohistochemistry (anti-BRP staining). (**D**) Maximal projection of 100 s GCaMP video (grey) overlaid with registered confocal BRP image (green). Red arrows indicate locations from which activity shown in (**E**) is read out. (**E**) Detail from black dashed rectangle in (**D**): Left: 500 ms sequence (16-color LUT, contrast adjusted) of a single spontaneous SV fusion event attributed to a single AZ (white circle). Yellow asterisks indicate AZ locations identified by BRP staining & confocal image. Center: event assignment by signal strength within the ROIs. GCAmp trace of the assigned AZs together with the signal at four neighboring AZs are shown. Right: Fluorescence traces from individual AZs in (**D**/**E**) during either spontaneous (orange) or AP-evoked (blue) recordings. (**F**) Cell-wise mean±SEM (N = 15 animals) fluorescence traces of 670 spontaneous and 2849 AP-evoked events. Arrows point to corresponding times indicated in (E) (dark red: 300 ms before peak, green: at the time of the peak, orange: 200 ms after the peak fluorescence). See also **Figure 1 - figure supplement 1&2**.

We first validated to which extent BRP serves as a reliable marker for the AP-responsive AZs we sought to investigate. Using the approach above, local activity maps for either transmission mode at BRP-positive AZs were generated for individual NMJs (**Figure 2A**). While some synapses only showed activity during either the spontaneous or AP-evoked recoding episode, others

127 contributed to both modes ("mixed" AZs) (**Figure 2 – figure supplement 3B)**. Merely observing
128 one type of activity during our recording does not preclude that these AZs might eventually also
129 engage in the other mode at later times or with additional stimuli. Indeed, longer experiments
130 increase the proportion of "mixed" AZs (Melom et al., 2013). However, it is unclear whether
131 eventually (for infinite recording time) all BRP-positive AZs would be expected to engage in
132 both transmission modes or whether some might be dedicated to spontaneous transmission only.
133 To investigate this, we used a survival analysis to extrapolate whether all BRP-positive AZs
134 observed to engage in spontaneous activity during the first recording episode would at some
135 point be expected to additionally be AP-responsive (considered as "death" of a dedicated
136 spontaneous synapse) or whether some AZs might never respond to APs (considered "immortal"
137 for infinite stimuli) (see methods for details). This analysis indicated that even though the
138 fraction of "spontaneous only" synapses decreased exponentially with time, our data was most
139 consistent with a plateau of 21% of AZs predicted to never respond to APs ("immortal"
140 spontaneous only AZ) (**Figure 2 – figure supplement 1**). This constitutes ~14% of all AZs
141 active throughout the experiment, similar to an estimate of a classic study at the frog NMJ
142 (Zefirov et al., 1995). Thus, while a small fraction of BRP-positive AZs appears dedicated to
143 spontaneous transmission, the vast majority (>85%) of active BRP-positive AZs are AP-
144 responsive (as expected from its role in organizing the AP-dependent release machinery).
145 Analyzing BRP-positive AZs therefore enables us to study the role of spontaneous transmission
146 at predominantly AP-responsive synapses.

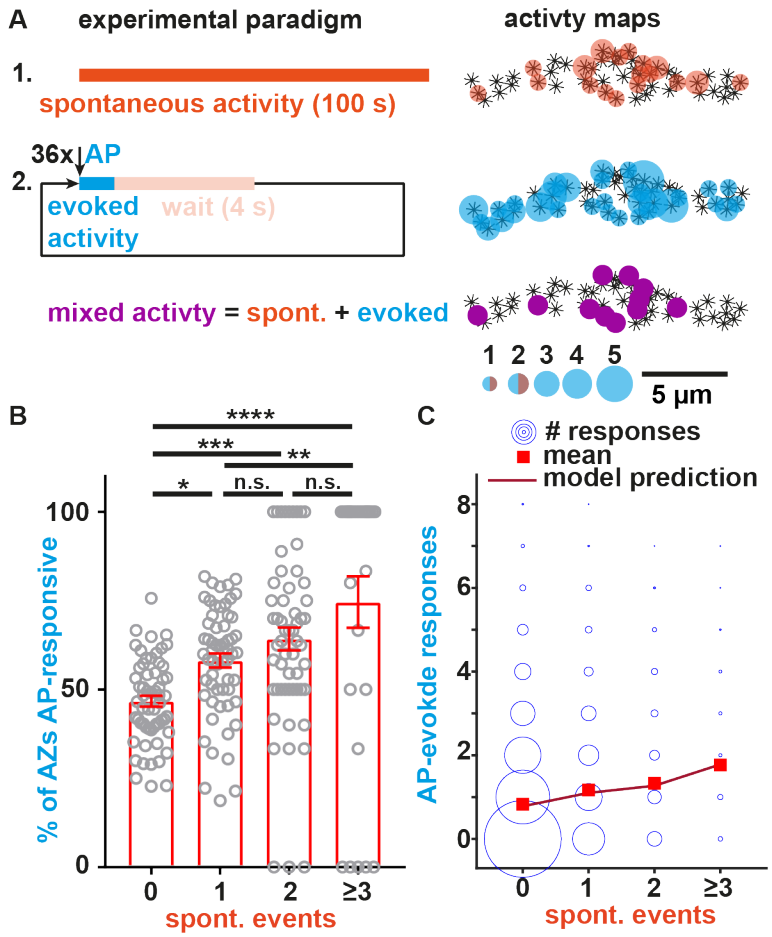

Figure 2. Spontaneous transmission at individual BRP-positive AZs predicts their AP-responsiveness. (**A**) Left: Experimental paradigm. Spontaneous events (top, orange) are recorded for 100 s in isolation before 36 APs are elicited at 0.2 Hz (middle, blue). AZs engaging in both modes during the recording show mixed activity (purple, bottom). Right: AZs of this NMJ are indicated as asterisks and were identified by anti-BRP immunostaining. The local activity profile is indicated by colored circles whose sizes represent the number of spontaneous (orange) or AP-evoked (blue) events (see legend). AZs with mixed activity are shown in purple. (**B**) Animal-wise (N=59 in total) comparison of the fraction of BRP-positive AZs responding to AP-stimulation shown for different numbers of spontaneous events detected at these AZs. Because of the overall low per-AZ activity, fewer animals are found in the groups with more spontaneous events (N(0)=59, N(1)=59, N(2)=58, N(≥3)=29, the group "≥3" pools the responses from AZs with 3 and 4 spontaneous events as only three animals had each one AZ with four spontaneous events). (**C**) Analysis of the relation between the observed AP-evoked and spontaneous transmission events at individual BRP-positive AZs. Events from all imaged AZs in the 59 animals are pooled. The size of the circles relates to the number of observations (between 1 and 3966). Red squares indicate mean number of evoked responses, the line indicates the model prediction (see methods). Number of BRP-positive AZs investigated: n(AZs)=9677, number of animals (N) as in (B). Bars in panel B indicate mean, error bars SEM. * <0.05; ** p<0.01; ***p<0.001; ****p<0.0001; n.s.: not significant. One-way ANOVA with post hoc Tukey's multiple comparisons test. See also **Figure 2 – figure supplement 1-3**.

166 We next investigated the relation between both transmission modes at the BRP-positive AZs. We
167 first tested to what extent spontaneous activity predicted the probability of AZs to respond to
168 APs. For this we plotted the fraction of AZs that showed activity at least once during the 36 AP
169 stimuli as a function of the spontaneous activity measured at those AZs prior to stimulation for
170 each animal (59 animals were investigated). This revealed that AZs with (more) spontaneous
171 activity were more likely to respond to APs (Fig. 2B).

172 We then went on to investigate whether the number of spontaneous events detected prior to
173 stimulation predicted the number of AP-induced responses at individual, BRP-positive AZs. For
174 this we evaluated the experimental data with a generalized linear model using a negative
175 binomial response distribution with a log link. The number of evoked events was modelled a
176 function of spontaneous events and a variable intercept was allowed for each animal (with a
177 random effect). The effect of the number of spontaneous events was strongly statistically
178 significant ($p < 0.0001$), demonstrating that AP-evoked transmission strongly depended on the
179 spontaneous activity. We furthermore found that a higher spontaneous activity at a given AZ
180 predicted more AP-evoked events (a significant monotonic trend was confirmed using a
181 nonparametric Mann-Kendal trend test, $p = 0.045$, for details see methods). Importantly, the
182 effect of the number of spontaneous events was also strongly statistically significant ($p < 0.0001$)
183 with a positive trend ($p = 0.045$) in separate experiments in which we first measured AP-evoked
184 activity and afterwards measured spontaneous activity (inverse sequence; **Figure 2 – figure**
185 **supplement 3A,B**), ruling out effects of e.g. activity run-down and fluorescence bleaching.
186 Thus, the spontaneous activity of evocable synapses at rest is a highly reliable predictor of their
187 responsiveness to AP-stimulation.

188 While above analysis demonstrated that AP-evoked responses of single SZs depended on their
189 spontaneous activity, we next wondered whether -inversely- AP-evoked transmission affected
190 spontaneous activity. To investigate this, we quantified the spontaneous activity "interleaved"
191 between AP-stimuli (**Figure 2 – figure supplement 3A**). While interleaved spontaneous events
192 had similar amplitudes as ones recorded separately, their frequency was strongly reduced
193 (frequencies – seq: 0.0037 Hz/AZ; int: 0.0018 Hz/AZ; N = 9 animals, p = 0.0003; amplitudes –
194 seq: 786.8 a.u.; int: 845.5 a.u.; N = 9 animals, p = 0.13; paired parametric two-tailed t-test).
195 Moreover, 39% fewer AZs were seen to engage in both transmission modes, while a larger
196 fraction of AZs solely responded to APs (**Figure 2 – figure supplement 3B**), indicating that AP-
197 stimulation reduces spontaneous transmission at AP-evokable AZs. As the only difference
198 between the two analyses is whether spontaneous activity is measured in isolation or in-between
199 APs, our results clearly demonstrate that AP-evoked transmission reduces spontaneous
200 transmission at BRP-positive AZs. Because this is unlikely due to saturation of NT receptors (see
201 below) this cross-depletion indicates the use of common presynaptic resources, including a
202 shared pool of SVs used for both transmission modes.

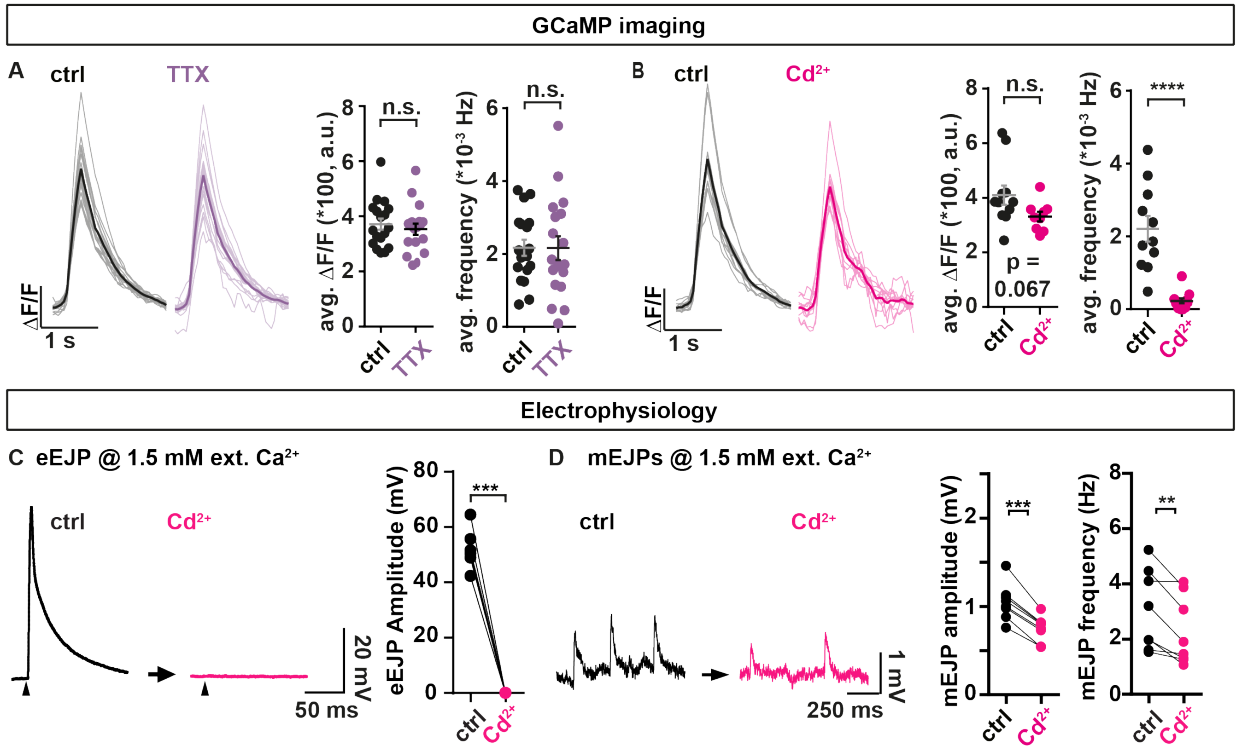

Figure 3. The non-specific voltage gated Ca^{2+} channel blocker Cd^{2+} affects spontaneous transmission. (**A&B**) analysis of spontaneous transmission using GCaMP-imaging at BRP-positive AZs to study the consequences of the voltage gated Na^{+} channel blocker TTX (purple, 1 µM) and the Ca^{2+} channel blocker Cd^{2+} (magenta, 740.7 µM). Left: Single cell mean (faint) and cell-wise average (solid) traces of spontaneous events. Right: Cell-wise quantification of GCaMP event amplitudes and event frequencies. (**C&D**) Assessment of the consequences of Cd^{2+}-application (300 µM, black→magenta) on AP-evoked eEJPs (C) and on spontaneous mEJPs (D) in paired current clamp recordings of muscle 4 NMJs. (C) Left: Representative eEJP before (black) and after (magenta) Cd^{2+} application. Arrowheads indicate time of stimulation. Right: Animal-wise quantification of eEJP amplitudes before (black) and after (magenta) Cd^{2+} application. (**D**) Left: Representative mEJC traces before (black) and after (magenta) Cd^{2+} (300 µM) application. Right: Cell-wise quantification of mEJC amplitudes and -frequencies. Number of animals in (A): N(ctrl) = 18; N(TTX) = 18. Number of animals in (B): N(ctrl) = 11; N(Cd^{2+}) = 11. Number of animals in (C&D): N=8. Horizontal lines in (A&B) indicate mean, error bars SEM. n.s. not significant; * $p<0.05$; *** $p<0.001$; **** $p<0.0001$. Two-tailed parametric Student's t-test for comparisons in A&B. Paired parametric t-test for comparisons in (C&D). See also **Figure 3 – figure supplement 1&-2**.

We previously found that both transmission modes were positively correlated to the AZ-levels of BRP and Unc13A (Reddy-Alla et al., 2017) and here sought to investigate whether a common molecular dependence extends further, to voltage gated Na^{+} and/or Ca^{2+} ion channels which trigger AP-evoked transmission. Application of the voltage gated Na^{+} channel blocker tetrodotoxin (TTX) did not affect the frequency of spontaneous events (**Figure 3A**), indicating

224 their independence from these channels. Instead, GCaMP imaging detected a strong reduction of
225 spontaneous activity upon application of the voltage gated Ca^{2+} channel blocker $CdCl_2$
226 (**Figure 3B**) (Ryglewski et al., 2012), which could implicate a dependence on these channels.
227 However, the GCaMP signals themselves also tended to be affected (a lower average amplitude
228 and slightly different kinetics of the GCaMP signals were seen, **Figure 3B**) which raises the
229 concern that Cd^{2+} may interfere with optical signal detection. We therefore complemented our
230 analysis with electrophysiological recordings, which -unlike our optical analysis at BRP positive
231 AZs of 1b boutons- sample spontaneous and AP-evoked events across the entire NMJ.

232 Current clamp recordings without current injection into the muscles monitor synaptic activity
233 while allowing the muscle's membrane potential to vary naturally with the transmission (similar
234 as in our optical recordings). Paired analyses of AP-evoked transmission at muscle 4 NMJs
235 revealed that Cd^{2+} fully blocked AP-evoked Excitatory Junction Potentials (eEJPs) (**Figure 3C**).
236 Comparison of spontaneously occurring miniature Excitatory Junctional Potentials elicited by
237 single SV fusion events before and after treatment revealed a reduction in both their amplitude
238 and frequency by Cd^{2+} (**Figure 3D**). This effect appeared specific to a blockage of Ca^{2+} influx by
239 Cd^{2+}, as Cd^{2+} had no effect on these measures in animals recorded in the absence of extracellular
240 Ca^{2+} **Figure 3 – figure supplement 1A** (and we excluded run-down as responsible for decreased
241 mEJP frequencies in this paradigm using a mock treatment) (**Figure 3 – figure supplement 1B**).
242 Thus, Cd^{2+} treatment clearly alters spontaneous transmission. However, whether the reduced
243 mEJPs frequency was (entirely) due to a decrease in spontaneous presynaptic NT release could
244 not be discerned with certainty due to the simultaneous decrease in mEJP amplitudes (which
245 could have reduced some events below our detection limit).

246 Decreased mEJP amplitudes could be due to a Cd^{2+}-dependent depolarization of the muscle's
247 resting membrane potential. We therefore additionally performed voltage clamp recordings
248 where this potential is set by the experimenter. In these we monitored spontaneous and AP-
249 evoked release by measuring the currents required to clamp this potential. This revealed a
250 decrease in the number of spontaneous events without a change of their amplitudes (**Figure 3 –**
251 **figure supplement 2**), thereby alleviating the concern that the decrease in spontaneous event
252 frequency is secondary to a in their amplitudes. Together, our electrophysiological analysis
253 confirms a partial dependence of spontaneous NT release on voltage gated Ca^{2+} channels.
254 However, the observed reduction of events following Cd^{2+} application was much smaller than in
255 the optical assay (compare **Figure 3B** and **Figure 3 – figure supplement 2**) which we attribute
256 to a large proportion of spontaneous NT release events from non-BRP positive locations (see
257 discussion).

258 While above experiments point to the use of common presynaptic resources, another question
259 pertains to the postsynaptic receptors that detect neurotransmitters that could either be segregated
260 or shared between transmission modes (**Figure 4A,B**). Due to the strong predictive value of
261 spontaneous activity for AP-evoked responses, spontaneous transmission might serve as a
262 continuous neural signal to monitor AP-sensitivity. If so, this "mixed" channel should activate
263 the same postsynaptic NT receptors (**Figure 4B**). To test this, we stimulated AP-evoked NT
264 release in the presence of the use-dependent glutamate receptor blocker Philanthotoxin (PhTx)
265 (Frank et al., 2006; Sara et al., 2011) and quantified whether this affected spontaneous
266 transmission (**Figure 4C**), which only happens if receptors are shared (**Figure 4A,B**).

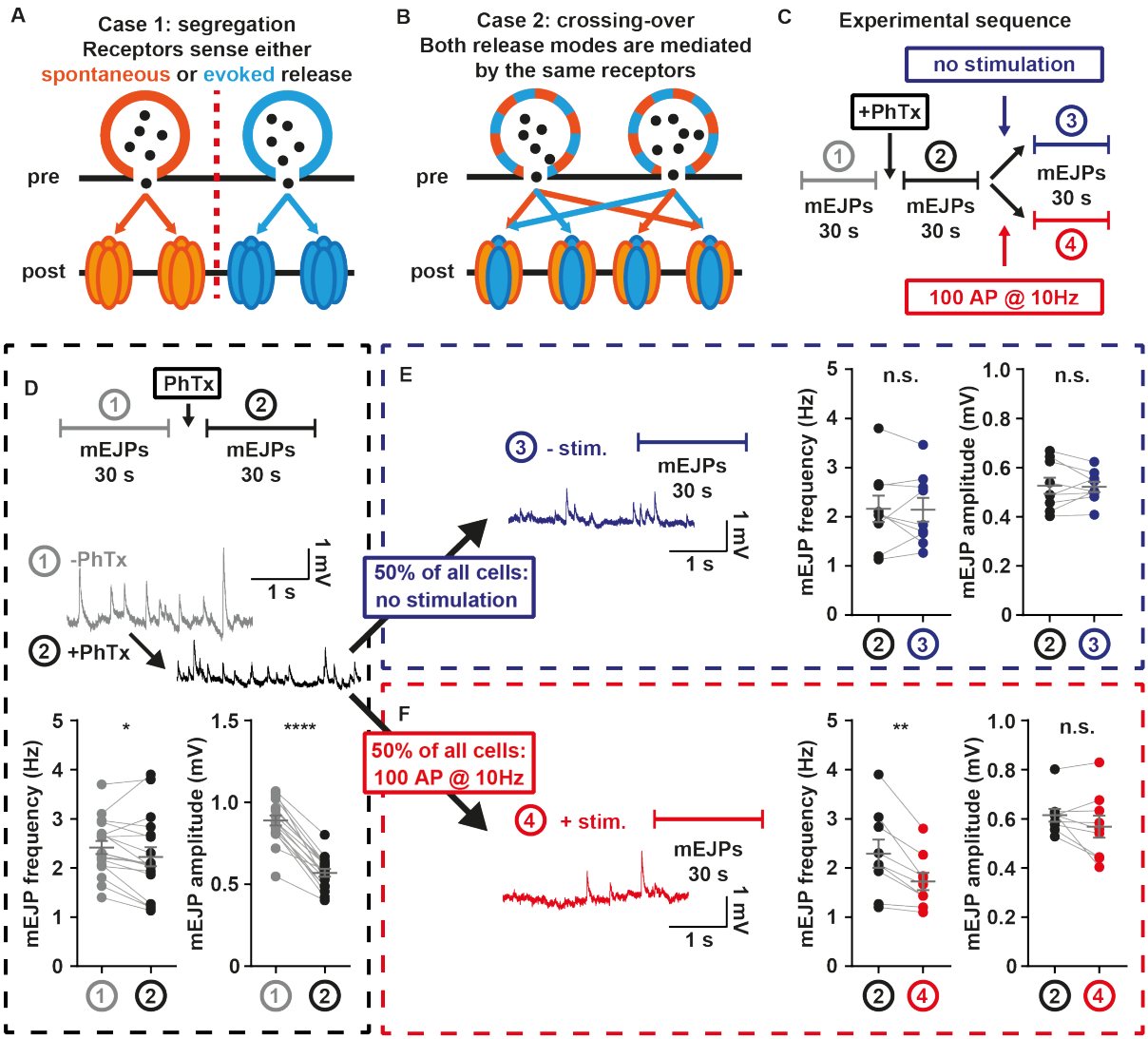

Figure 4 Postsynaptic receptors share sensitivity for both release modes. (**A**) Illustration case 1: Spontaneous (orange) and AP-evoked (blue) transmission rely on distinct postsynaptic receptors. (**B**) Illustration case 2: Both release modes use the same postsynaptic receptors. (**C**) Experimental setup: After 30 s mEJP baseline recordings, larvae are treated with 4 µM PhTx, and spontaneous mEJPs are recorded for another 30 s. Then, one half of animals (measurement 4, red) undergoes stimulation at 10 Hz over 10 s, the other half (measurement 3, blue) receives no stimulation. Another 30 s of mEJPs are recorded, yielding traces as shown in (D-F). (**D**) mEJP frequency and amplitude quantification before (grey; measurement 1) and after (black; measurement 2) PhTx application (N = 18 animals) (**E**) mEJP frequency and amplitude quantification after PhTx application and without stimulation (N = 9 animals) (**F**) mEJP frequency and amplitude quantification after PhTx application and with stimulation (N = 9 animals). Means are shown, error bars indicate SEM. n.s. not significant; * $p<0.05$; ** $p<0.01$; **** $p<0.0001$, paired t-test See also **Figure 4 – figure supplement 1**.

281 We initially monitored baseline spontaneous transmission in electrophysiological current-clamp
282 experiments for 30 s before and after PhTx application, which expectedly reduced the amplitude
283 of postsynaptic "miniature" excitatory junction potentials (mEJPs) caused by spontaneous NT
284 release (**Figure 4D**)(Frank et al., 2006). In half of the animals, the efferent nerve was then
285 stimulated with 100 APs (10 Hz, **Figure 4F**), a stimulation suitable to block glutamate receptors
286 in the presence of PhTx (**Figure 4 – figure supplement 1**). The other half of the animals
287 received no AP stimulation (but saw a corresponding 10 s wait) (**Figure 4E**). In both groups,
288 mEJPs were recorded for another 30 s. If spontaneous and AP-evoked activity were exclusively
289 sensed by distinct postsynaptic receptors (**Figure 4A**), AP-stimulation should not affect
290 spontaneous transmission. Contrasting this, a clear decrease of mEJP frequency selectively
291 occurred in the group receiving the AP stimulations (**Figure 4F**). The effect was specific to the
292 use-dependent block by PhTx, as stimulation alone had no effect (**Figure 4 – figure**
293 **supplement 1A-C**), arguing against SV pool depletion or receptor desensitization as underlying
294 cause. Our results show that receptor block induced by AP-evoked activity affects spontaneous
295 neurotransmission, clearly indicating that both transmission modes activate the same receptors at
296 AP-evocable synapses. This does not exclude the existence of additional "distinct"
297 communication channels (i.e. ones dedicated to spontaneous transmission) but demonstrates that
298 both transmission modes share NT receptors at AP-responsive AZs.

299

300 ## Discussion

301 Our data demonstrate that the spontaneous activity of individual AP-evocable AZs is a predictor
302 of their responsiveness to AP stimuli. This functional property could enable synapses to
303 continuously monitor the evocable signal strength of a connection at rest, using highly uniform,
304 spontaneous signals ("pings") and would allow for detection and homeostatic compensation of
305 dysbalances even before the connection is stimulated. Indeed, presynaptic homeostatic
306 potentiation at the *Drosophila* NMJ increases NT release to compensate reduced postsynaptic
307 NT receptor sensitivity by entirely relying on spontaneous (not AP-induced) activity (Frank et
308 al., 2006). Such mechanisms may even be more important for sparsely activated synaptic
309 connections of the central nervous system and indeed this homeostasis also exists in the
310 mammalian brain (Delvendahl et al., 2019).

311 The easiest explanation for the high interdependence of both activity modes at AP-responsive
312 AZs is a reliance on the same machinery. We find that both transmission modes activate shared
313 NT receptors because AP-stimulation in the presence of the use-dependent PhTx (but not AP-
314 stimulation alone) decreased spontaneous transmission (**Figure 4, Figure 4 – figure supplement**
315 **1A-C**). A previous study using PhTx at the *Drosophila* NMJ concluded no effect of AP-
316 dependent NT receptor block on spontaneous transmission (Peled et al., 2014). However, those
317 experiments were compared across different groups of animals (which is less sensitive) and were
318 performed over far longer times (25 min vs. 10 s here) during which compensatory, homeostatic
319 mechanisms take place with this treatment (Frank et al., 2006; Davis and Müller, 2015; Harris
320 and Littleton, 2015).

321 We show that AP-stimulation reduces spontaneous activity (**Figure 2 – figure supplement 3B**).
322 This could indicate the saturation or depletion of a common pre- or postsynaptic resource. It
323 seems unlikely that this effect is caused by the saturation of postsynaptic NT-sensing receptors
324 because even stronger AP-stimulation (100 APs @ 10 Hz) elicited no detectable effect on the
325 rate of spontaneous transmission in electrophysiological recordings (**Figure 4 – figure**
326 **supplement 1A-C**). Instead, it is more likely that the AP-induced reduction of spontaneous
327 activity is due to a depletion of a common pool of SVs for both transmission modes (Groemer
328 and Klingauf, 2007; Hua et al., 2010; Wilhelm et al., 2010). This implies a long-lasting
329 inhibition of spontaneous activity recovering much slower rate of pool refilling than current
330 estimates (Miki et al., 2016; Kobbersmed et al., 2020). The precise reason for this is unknown
331 but may reflect a difference in such experiments that typically engage repetitive stimuli vs. the
332 sparse stimulation used here (0.2 Hz).

333 Previous analyses indicated that both spontaneous and AP-evoked single-AZ activity were
334 positively related to the local levels of BRP and Unc13A (Reddy-Alla et al., 2017). The common
335 requirement on presynaptic proteins likely extends further as mutations of specific residues of
336 SNAP25 or Syaptotagmin-1 (which both mediate AP-evoked activity) reduced both transmission
337 modes (Xu et al., 2009; Weber et al., 2010). We here investigated whether a common
338 dependence at the *Drosophila* NMJ also extended to voltage gated ion channels. While blocking
339 voltage gated Na^+ channels with TTX (which abolishes AP-evoked release) did not affect
340 spontaneous transmission, we saw a strong reduction spontaneous transmission upon application
341 of the non-specific voltage gated Ca^{2+} channel blocker Cd^{2+} in our GCaMP experiments
342 (**Figure 3B**). This could mean that stochastic gating of VGCCs triggers spontaneous
343 transmission by activating the same fusion machinery at AP-evocable AZs. Indeed, such a

344 reliance of spontaneous activity on VGCCs has been demonstrated for other systems (Shahrezaei
345 et al., 2006; Goswami et al., 2012; Ermolyuk et al., 2013). However, whether this is also the case
346 for *Drosophila* synapses is debated. An argument against this is that unlike in other systems
347 electrophysiologically measured spontaneous release rates at the *Drosophila* NMJ do not depend
348 on the external Ca^{2+} concentration (Huntwork and Littleton, 2007; Xu et al., 2009; Groffen et al.,
349 2010; Goel et al., 2017). However, one reason for this discrepance could relate to the locations of
350 the spontaneous events predominantly detected using either approach.

351 In our GCaMP imaging analysis we specifically focus on spontaneous transmission from BRP-
352 positve AZs, which are predominantly AP-resposnive (**Figure 2 – figure supplement 1**),
353 therefore represening a "mixed channel" with both transmission modes. In contrast,
354 electrophysiological recordings assess spontaneous transmission across the entire NMJ and
355 therefore can additionally detect spontaneous transmission from synaptic contacts with no (or
356 non-detectable) BRP. Indeed, our electrophysiological recordings demonstrated a much smaller
357 inhibition of spontaneous activity by Cd^{2+} than seen with GCaMP imaging (**Figure 3B&D,**
358 **Figure 3 – figure supplement 2**). This much reduced sensitivity could imply that synapltic
359 connections without (or with low) BRP form a "dedicated spontaneous" communciation channel
360 which might dominate overall spontaneous transmission at the NMJ. In fact, these ("non-BRP
361 localized") events could well represent the "dedicated communication channel" for spontaneous
362 transmission shown to utilize distinct SVs, NT receptors, SNAREs (vti1a, VAMP7) and Ca^{2+}
363 sensors (doc2b) and therefore might not be prone to manipulation of the AP-evoked machinery
364 (Sara et al., 2005; Fredj and Burrone, 2009; Groffen et al., 2010; Ramirez et al., 2012; Bal et al.,
365 2013). This may also explain some of the differences (opposite dependence on BRP, inverted
366 correlation of signals) we observe to the study by Peled and colleagues who had studied GCaMP

367 events throughout the NMJ in a null mutant of Rab3 where the spatial segregation of BRP-
368 positive and BRP-negative areas is augmented (Graf et al., 2009; Peled et al., 2014).

369 What may determine the ratio of spontaneous events in the "mixed" or "separate"
370 communication channel? This could, for instance, relate to a developmental trajectory, with
371 nascent synapses forming the "dedicated spontaneous channel" where a specialized machinery
372 first mediates the spontaneous NT release needed for maturation which at later times leads to the
373 accumulation of the AP-responsive release machinery, generating the "mixed channel"
374 (Truckenbrodt and Rizzoli, 2014; Walter et al., 2014; Akbergenova et al., 2018). In that case, the
375 ratio between the two channels might greatly depend on the maturity of the model system and
376 indeed spontaneous activity decreases and evoked transmission increases during maturation of
377 neural cultures (Andreae et al., 2012). Thus, some of the differences reported in the literature
378 regarding the in- or interdependence of transmission modes may rely on different states of
379 maturation of the systems in which experiments were performed (e.g. between cultured neurons,
380 brain slices or NMJs). Likewise, genetic deletion of synaptic components of the AP-evoked
381 machinery may impede this transition in addition to their effect on communication along the
382 "mixed" channel thereby increasing the proportion of events in the "dedicated spontaneous"
383 channel. This may partly explain the divergent effects on both transmission modes upon null-
384 mutation of genes encoding the synaptic proteins Synaptobrevin, Synaptotagmin-1, complexin or
385 voltage gated Ca^{2+} channels (Littleton et al., 1993; Broadie et al., 1994; Geppert et al., 1994;
386 Broadie et al., 1995; Deitcher et al., 1998; Reim et al., 2001; Schoch et al., 2001; Huntwork and
387 Littleton, 2007; Hou et al., 2008; Martin et al., 2011; Yang et al., 2013). Thus, while our study
388 identifies shared resources and a clear predictive role of spontaneous transmission for AP-evoked
389 transmission in the "mixed channel", the functional relevance of the relation between "dedicated

390 spontaneous" and "mixed" transmission channels for synapse development, maintenance, and
391 information transfer demand further investigation.

392 # Materials & Methods

393 ## Resources Table

REAGENT or RESOURCE	SOURCE	IDENTIFIER
Antibodies		
primary: mouse anti BRP$^{c\text{-}term}$	Developmental Studies Hybridoma Bank	Cat# nc82, RRID:AB_2314866
primary: rabbit anti BRP^{last200}	Ullrich et al., 2015	n/a
secondary: donkey anti guinea pig DyLight 405	Jackson ImmunoResearch	Cat# 106-475-003, RRID: AB_2337432
secondary: goat anti mouse Cy3	Jackson ImmunoResearch	Cat# 115-165-146, RRID: AB_2338690
secondary: goat anti rabbit Cy3	Jackson ImmunoResearch	Cat# 111-165-144, RRID: AB_2338006
Experimental Models: Organisms/Strains		
D. melanogaster: Wild type: *w1118*	own lab stock	n/a
D. melanogaster: Mhc-myr-gcamp5g/III	Reddy-Alla et al., 2017	n/a
Software and Algorithms		
MATLAB	Mathworks Inc.	R2016b
ImageJ	NIH	v1.48q/v1.52i
MicroManager	https://micro-manager.org	v1.4.2
Custom MATLAB code	this paper/Reddy-Alla et al., 2017	n/a
Custom ImageJ code	this paper/Reddy-Alla et al., 2017	n/a
LAS AF Lite	Leica Microsystems	v2.6.3
LAS X	Leica Microsystems	n/a
Clampfit	Molecular Devices	v10.5/10.6.2.2
Graphpad Prism	GraphPad Software	v6.01

Pharmacological agents		
Philanthotoxin-433	Sigma Aldrich	Cat# P207
Cadmium dichloride	Sigma Aldrich	Cat# 202908
EGTA tetrasodium salt	Sigma Aldrich	Cat# E8145
Other		
Leica SP8 confocal microscope	Leica Microsystems	n/a

394

395 **Animal rearing and preparation**

396 Experiments making use of genetically modified invertebrate animals have been registered with
397 and approved by the respective authorities (Landesamt für Gesundheit und Soziales LaGeSo,
398 Berlin), and were performed in accordance with German laws and regulations on biosafety.
399 Animals were bred and maintained at standard laboratory conditions (Sigrist et al., 2003) on
400 semi-defined fly medium (Bloomington recipe). Male and female flies were used for all
401 experiments. Wild type *w1118* flies were used for the electrophysiology experiments shown in
402 **Figure 3C&D, Figure 3 – figure supplement 1&2, Figure 4, and Figure 4 – figure**
403 **supplement 1**. The following fly strain was used for all other experiments: *Mhc-*
404 *myrGCaMP5G/+;* (Reddy-Alla et al., 2017). Third instar larvae were dissected as described in
405 Qin et al., 2005 in standard Ca^{2+}-free, hemolymph-like solution HL-3 (composition in mM: 70
406 NaCl, 5 KCl, 20 $MgCl_2$, 10 $NaHCO_3$, 5 Trehalose, 115 Sucrose, 5 HEPES; Stewart et al., 1994;
407 low Mg^{2+}-solution used for PhTx-electrophysiology experiments contained 10 mM $MgCl_2$),
408 adjusted to pH=7.2. Dissection was performed using fine insect pins on Sylgard-184 (Dow
409 Corning, Midland MI, USA), by opening the dorsal body wall from posterior to anterior,
410 removing all internal organs, and severing the motoneurons from the CNS without damaging the
411 underlying body wall muscles, then removing the brain. For experimentation, the dissected

412 larvae were then transferred to recording chambers on the respective recording setups, as detailed
413 in the sections explaining electrophysiology and live calcium imaging.

414

415 **Electrophysiology**

416 All electrophysiological experiments were performed at room temperature using sharp glass
417 electrodes (borosilicate glass with filament, 0.86x1.5x80 nm, Science products, Hofheim,
418 Germany) pulled with a Flaming Brown Model P-97 pipette puller (Sutter Instruments, CA,
419 USA). Stimulating suction electrodes were pulled on a DMZ-Universal Puller (Zeitz-Instruments
420 GmbH, Germany) and fire polished using a CPM-2 microforge (ALA Scientific, NY, USA).
421 Recordings were performed in current clamp mode at muscle 6 (PhTx experiments) / muscle 4
422 (Cd^{2+}/TTX experiments) in segments A2/A3 as previously described (Zhang and Stewart, 2010)
423 using an Axon Digidata 1550A digitizer, Axoclamp 900A amplifier with HS-9A x0.1 headstage
424 (Molecular Devices, CA, USA) and on a BX51WI Olympus microscope with a 40X
425 LUMPlanFL/IR water immersion objective. Sharp intracellular recording electrodes with a
426 resistance of 20-35 MΩ were made and back-filled with 3 M KCl. Only cells with membrane
427 potentials below -60 mV (PhTx experiments) / -40 mV (Cd^{2+} experiments) and membrane
428 resistances greater than 4 MΩ were considered. Recordings were acquired using Clampex
429 software (v10.5) and sampled at 10-50 kHz, filtering with a 5 kHz low-pass filter. Analysis for
430 all electrophysiological datasets was performed with Clampfit (v10.5/10.6.2.2) and Graphpad
431 Prism 6 software. mEJPs were further filtered with a 500 Hz Gaussian low-pass filter. A single
432 mEJP template was generated for each cell and used to identify individual mEJPs, and to
433 calculate the mean mEJP amplitude and frequency per cell.

434 **Current clamp experiments to determine VGCC role in spontaneous SV release**

435 Current clamp recordings using $CdCl_2$ in order to block VGCCs were performed at room
436 temperature from muscle 4 of abdominal segments A2-A4 (**Figure 3C&D, Figure 3 – figure**
437 **supplement 1**) using 2 ml standard HL3 medium containing either 1.5 mM $CaCl_2$
438 **(Figure 3C&D, Figure 3 – figure supplement 1C&D)** or 0 mM $CaCl_2$ together with 2 mM of
439 the Ca^{2+} chelator EGTA-tetrasodium salt (Sigma, Germany, E8145) to buffer residual Ca^{2+} traces
440 **(Figure 3 – figure supplement 1A&B)**. Recordings shown in **Figure 3C&D, Figure 3 – figure**
441 **supplement 1** were obtained before and after the addition 300 µM $CdCl_2$ (magenta) or the
442 equivalent volume of dH_2O as control (grey) (see pharmacology section) in a strictly paired
443 fashion. In detail, starting with a $CdCl_2$-free extracellular medium ("ctrl") a single AP was
444 evoked in motoneurons (8 V, 300 µs pulse) using an ISO-STIM 01D stimulator (NPI Electronic,
445 Germany) followed by a 30 s resting period. Sequentially, spontaneous mEJPs were recorded for
446 30 s followed by an immediate exchange of 1 ml bath solution (2 ml total bath volume) by 600
447 µM $CdCl_2$-HL3 ("Cd^{2+}") or dH_2O-HL3 ("ctrl") within a resting period of 2 min. Afterwards,
448 another single AP was evoked followed by 30 s rest and recording of 30 s spontaneous activity.
449 eEJP amplitudes were determined by quantifying the maximal voltage deflection from the
450 basline following an AP (values in the standard noise range were considered as zero).

451 **Two-electrode voltage clamp experiments to determine VGCC role in spontaneous SV**
452 **release**

453 TEVC recordings were performed at room temperature from muscle 4 of abdominal segments
454 A2-A4 (**Figure 3 – figure supplement 2**). Signals were recorded using a 5 KHz low-pass filter
455 at a sampling frequency of 20 KHz using the Digidata 1440A digitizer (Molecular devices,
456 Sunnyvale, CA, USA) with Clampex (v10.6) software and Axoclamp 900A amplifier (Axon

457 instruments, Union City, CA, USA) with Axoclamp software. Only cells with resting membrane
458 potentials below -49 mV and membrane resistances above 4 MΩ prior to measurements were
459 included in the datasets. TEVC recordings shown in **Figure 3 – figure supplement 2** were
460 performed at 1.5 mM extracellular $CaCl_2$. Recordings shown in **Figure 3 – figure supplement 2**
461 were obtained in the presence of 740.7 µM $CdCl_2$ (magenta) or the equivalent volume of dH_2O
462 as control (black) (see pharmacology section). Cells were clamped at a holding potential of -55
463 mV.

464 **Current clamp experiments to determine receptor sensitivity to different SV release modes**

465 For current clamp experiments using PhTx to determine postsynaptic receptor field sensitivity to
466 both release modes (**Figure 4**), the Sylgard block and completed larval preparation was placed in
467 the recording chamber which was filled with 2 ml HL3 (0.4 mM $CaCl_2$, 10 mM $MgCl_2$). eEJPs
468 were recorded by stimulating the appropriate nerve at 10 Hz, 100 times (8 V, 300 µs pulse) using
469 an ISO-STIM 01D stimulator (NPI Electronic, Germany).

470 Spontaneous mEJPs for analysis shown in **Figure 4D-F** and **Figure 4 – figure supplement 1A-**
471 **C** were recorded for 30 seconds. 1 ml of solution was then removed from the bath without
472 disturbing the preparation or electrodes and 1 ml of HL3 added containing PhTx-433 (Sigma-
473 Aldrich, MO, USA), mixing gently with the pipette to a final bath concentration of 4 µM PhTx.
474 Spontaneous mEJPs were recorded immediately, again for 30 seconds. Stimulation was
475 performed at 10 Hz for 10 seconds to measure eEJPs or, in the case of control recordings, 10
476 seconds passed without stimulation. Finally, mEJPs were recorded for 30 seconds. Recordings
477 shown in **Figure 4 – figure supplement 1A-C** were performed as above, using HL3 lacking
478 PhTx-433, as the exchange solution.

479 **Pharmacology**

480 Philanthotoxin (PhTx-433) used for experiments in **Figure 4** was obtained from Sigma Aldrich
481 (subsidiary of Merck KGaA, Darmstadt, Germany) and diluted to a stock concentration of 4 mM
482 in dH_2O. In experiments, it was used at a concentration of 4 µM in HL-3 by applying it directly
483 to the bath (see electrophysiology method section). Tetrodotoxin-citrate (TTX) used for
484 experiments shown in **Figure 3A** was obtained from Tocris (subsidiary of Bio-Techne,
485 Minneapolis, MN, USA) and diluted in dH_2O to a stock concentration of 1 mM. In GCaMP
486 experiments, it was used at a concentration of 1 µM in HL-3 (5 µL 1 mM TTX/dH_2O stock in
487 4.6 mL HL-3 and 0.4 mL dH_2O (diluting the HL-3 components to (in mM): 64.4 NaCl, 4.6 KCl,
488 18.4 $MgCl_2$, 9.2 $NaHCO_3$, 4.6 Trehalose, 105.8 Sucrose, 4.6 HEPES)), and imaging began after
489 2 minutes of incubation time. Cadmium dichloride ($CdCl_2$) was obtained from Sigma Aldrich.
490 For the experiments shown in **Figure 3B** a stock solution with a concentration of 10 mM was
491 made and for experiments further diluted to a final concentration of 740.7 µM in HL-3 (1.12 mL
492 10 mM $CdCl_2$/dH_2O stock in 14 mL HL-3 and a corresponding amount of 1.12 mL dH_2O in
493 14 mL HL-3 controls, diluting the HL-3 components to (in mM): 64.8 NaCl, 4.63 KCl, 18.52
494 $MgCl_2$, 9.26 $NaHCO_3$, 4.63 Trehalose, 106.48 Sucrose, 4.63 HEPES); measurements began after
495 2 minutes of incubation time. The Current Clamp experiments depicted in **Figure 3C&D** and
496 **Figure 3 – figure supplement 1** were performed at a later time. For these, a different stock
497 solution was made with a concentration of 300 mM in dH_2O, and used at a final concentration of
498 300 µM in HL-3 for electrophysiological experiments. Control experiments shown in **Figure 3 –**
499 **figure supplement 1C&D** were performed using the same amounts of the respective solvent
500 ($CdCl_2$: dH_2O/HL3, PhTx: dH_2O).

501

502 **Live Calcium-Imaging**

503 GCaMP live imaging experiments were conducted in 2 mL HL-3 containing 1.5 mM $CaCl_2$
504 (except for Ca^{2+}-titration in **Figure 1 – figure supplement 1H**: 0.4, 0.75, 1.5, 3, 6, 12 mM) on
505 an Olympus BX51WI epifluorescence microscope, using a water immersion LUMFL 60x 1.10 w
506 objective. A Lambda DG-4 (Sutter Instrument Company, Novato CA, USA) white light source
507 was used to illuminate the samples through a GFP excitation/emission filter set. For experiments
508 in **Figure 1 – figure supplement 1H** and **Figure 2 – figure supplement 1D-H**, a newer light
509 source of the same model was used in combination with an Olympus ND25 neutral density filter.
510 Images were acquired in camera-native 16-bit grayscale using an Orca Flash v4 sCMOS camera
511 (Hamamatsu Photonics, Hamamatsu, Japan) under constant illumination with an exposure of
512 50 ms per frame, resulting in an effective imaging frame rate of 20 Hz. For all GCaMP analysis,
513 spontaneous events were recorded from 1b NMJs in muscle 4, abdominal segments 2-4, for 100 s
514 (120 s in the case of TTX and Cd^{2+} experiments shown in **Figure 3A&B**). For experiments
515 involving the imaging of AP-induced ('evoked') events, the efferent motoneuronal axon bundle
516 innervating the same muscle was sucked into a polished glass capillary containing bath HL-3.
517 The glass capillary was held in place by a patch electrode holder (npi electronic, Tamm,
518 Germany), and contained a chlorided silver wire electrode, which connected to a pipette holder
519 (PPH-1P-BNC, npi electronic, Tamm, Germany). After recording of spontaneous events, 36
520 single stimuli were applied as a square depolarization pulse of 300 µs at 7 V, 0.2 Hz for 180 s
521 using a connected S48 stimulator (Grass Technologies, now part of Natus Medical Inc.,
522 Pleasanton, CA, USA), except for analysis shown in **Figure 2 – figure supplement 2**, where the
523 experimental sequence was reversed. Imaging start/end was controlled by µManager software
524 (version 1.4.20, https://micro-manager.org), and stimulation was administered through software

525 (Clampex 10.5.0.9, Molecular Devices, San Jose, CA, USA) controlling a DA/AD converter
526 (DigiData 1440A, Molecular Devices, San Jose, CA, USA). All videos acquired in 16-bit were
527 then converted to 8-bit using ImageJ (version 1.48q). See section Image processing and analysis
528 for further procedures and details.

529

530 **Immunohistochemistry**

531 After live imaging experiments, larval tissue was fixated for 10 min at RT using fresh 4% PFA in
532 0.1 mM PBS. Fixated samples (max. 8 per 1.5 mL sample cup) were then stored in 1 mL 1xPBS
533 until all samples had been collected, but 6 hours at most. Then, off-target epitope blocking was
534 performed in 1xPBS containing 0.05% Triton-X100 (PBS-T) and 5% normal goat serum (NGS)
535 (total volume: 1000 µL) for 45 min on a wheel at RT, 17 rpm. Immediately after, the mix was
536 replaced by an identical mixture and the respective first antibody was added at the following
537 concentrations: mouse $BRP^{C\text{-}term}$ (1:1000, Developmental Studies Hybridoma Bank, University
538 of Iowa, Iowa City, IA, USA), rabbit $BRP^{last200}$ (1:1000) (Ullrich et al., 2015). Samples were
539 incubated with the primary antibody overnight (15-16 h) at 4°C on a sample wheel. Afterwards,
540 samples were washed four times in PBS-T for 30 min at RT. Secondary antibodies were applied
541 (4 h, RT) in PBS-T containing 5% NGS at the following concentrations: donkey anti guinea pig
542 DyLight 405 (1:500, Jackson ImmunoResearch, West Grove, PA, USA), goat anti mouse Cy3
543 (1:500, Jackson ImmunoResearch), goat anti rabbit Cy3 (1:500, Jackson ImmunoResearch, West
544 Grove, PA, USA). After this, they were washed with PBS for 30 min and finally mounted on
545 26x76 mm glass slides (Paul Marienfeld GmbH, Lauda-Königshofen, Germany) in VectaShield
546 (Vector Laboratories, subsidiary of Maravai Life Sciences, San Diego, CA, USA) under 18x18
547 mm cover glass slides (Carl Roth GmbH, Karlsruhe, Germany) using clear nail polish to seal off

548 the sides of the cover glass slide. The samples were then stored at 4°C and imaged within a week
549 as described in the confocal microscopy and image processing section.

550

551 **Confocal microscopy and image processing**

552 Confocal imaging of immunohistochemically stained samples was performed on a Leica SP8
553 confocal quadruple solid-state laser scanning system (excitation wavelengths: 405, 488, 552, 635
554 nm), and operating on LAS X software (Leica Microsystems, Wetzlar, Germany) with a 63x 1.4
555 NA oil immersion objective at room temperature. Pixel edge length was 100 nm at a zoom factor
556 of 1.8 and a z-step size of 0.5 µm for all datasets. Care was taken to choose fluorophores with
557 non-overlapping excitation/emission spectra (see immunohistochemistry section), and confocal
558 GCaMP images were always acquired without additional IHC at 488 nm excitation. Single z-
559 stack images from all channels were exported from the proprietary .lif-format into TIF images
560 using LAS AF Lite software (version 2.6.3, Leica Microsystems, Wetzlar, Germany) and
561 converted to 8-bit grayscale maximal projections using custom ImageJ/Fiji software (version
562 1.52i, available upon request).

563

564 **Image processing and analysis**

565 **Stabilization of live-imaging videos**

566 As further analysis of GCaMP live-imaging videos was highly reliant on a stable position of the
567 NMJ over time, all 2D-translational movement (in x,y-direction) of the muscle during the
568 recording had to be corrected for. This was done as shown in Reddy-Alla et al., 2017, and is

569 described in the following. Converting videos of mhc-myr-GCaMP5G from 16-bit to 8-bit
570 grayscale was done in ImageJ.

571 After conversion from 16-bit to 8-bit, the 8-bit multipage .TIF-video file ('stack') was loaded
572 into MATLAB and a subregion of the first frame, containing the whole GCaMP-positive 1b
573 NMJ, was chosen as a reference for the registration process using the MATLAB function *getrect*.
574 Using the MATLAB function *normxcorr2*, every subsequent frame was then 2D-translated by a
575 simple *x,y*-shift until the highest cross-correlation between pixel values of the current frame and
576 the first frame was achieved. This procedure was repeated for all pairs of the first frame and
577 succeeding frames. For this procedure, all images were Gaussian filtered (MATLAB function
578 *imgaussfilt*) with a sigma value of 5 for noise reduction.

579 **Alignment of confocal images to live-imaging videos**

580 Next, we compensated for fixative-induced anisotropic deformation, orientation and size changes
581 in confocal images by registering them to GCaMP-videos in ImageJ using the plugin
582 "TurboReg" (Biomedical Imaging Group, EPFL, Switzerland; Thévenaz et al., 1998). An affine
583 transformation that used three reference points in each image applied *x,y*-translation, rotation,
584 and *x,y*-shearing where necessary to get the optimal overlay between GCaMP-signal in confocal
585 and live-imaging. In rare instances, a bilinear transform using 4 reference points was necessary
586 to achieve sufficient overlay between confocal image and GCaMP video. The necessary
587 transformation found for the confocal GCaMP image was then applied identically to all other
588 channels.

589 **Quantification of single AZ activity-levels**

590 In order to quantify protein and activity levels on the level of single AZs, we first defined ROIs
591 in the confocal BRP channel by applying the ImageJ function *find maxima* using threshold
592 values between 10 and 20. Circular ROIs with a diameter of 650 nm were centrally overlaid at all
593 *x,y*-positions found with this procedure. The integrated density (sum of intensities of all pixels
594 whose sub-pixel center lay within the borders of the circle) in all ROIs was then saved for each
595 confocal frame and live-imaging frame in .xls-format for later analysis in MATLAB.
596 Additionally, a file with all corresponding *x,y*-coordinates of all ROIs was saved as a text file.
597 Further, to correct for unspecific background fluorescence decay due to photobleaching, we
598 shifted all ROIs to a region without GCaMP fluorescence and generated another .xls-file
599 containing the fluorescence values in these ROIs over time. These values were later subtracted
600 from the corresponding fluorescence signal in the original ROIs.

601 We then loaded these files into MATLAB for further analysis. First, we determined all inter-AZ
602 distances (all distances between every possible pair of AZs) using the squared Euclidean distance
603 as shown in equation (1).

604 (1) $dist(ROIa, ROIb) = sz_{px} * \sqrt{(d_x(ROIa, ROIb))^2 + (d_y(ROIa, ROIb))^2}$

605 In equation (1), $ROIa$ and $ROIb$ are any of the determined ROIs, sz_{px} is the physical pixel edge
606 length of $0.108\overline{33}$ µm, and d_x and d_y are the vertical or horizontal pixel shift values in *x* or *y*,
607 respectively, between both compared ROIs. This resulted in a diagonally symmetrical matrix of
608 all possible inter-AZ distances. This distance was then used to exclude detecting another event
609 within 2.5 µm (evoked activity measurements) or 1000 µm (spontaneous activity measurements)
610 around one event in the same frame. We added another layer of security to exclude the detection

611 of the same event twice by only considering the ROI with the highest amplitude within the given
612 distance threshold and a single frame (each frame representing 20 ms of recording time).

613 The GCaMP fluorescence over time of each ROI was corrected for photobleaching as described
614 before, by subtracting the fluorescence measured in the corresponding background ROI. We then
615 performed a linear fit on each single fluorescence trace over time (separately for spontaneous and
616 AP-evoked activity recordings), yielding two parameters reflecting its slope and y-intercept
617 (MATLAB function *polyfit*). Using these parameters (slope s and y-intercept int), we performed
618 a baseline correction for each time step t and each ROI as shown in equation (2).

619 (2) $Fluo_{GCaMP,corr}(t, ROI) = Fluo_{GCaMP}(t, ROI) - (t * s(ROI) + int(ROI))$

620 A custom procedure was then used to detect single peaks in the resulting fluorescence traces. All
621 fluorescence traces were filtered by a 1D-filter using the MATLAB function *filter* (filter width: 5
622 frames). We then manually evaluated all instances in the fluorescence trace where the mean of
623 the unfiltered signal over three consecutive frames exceeded a threshold of four times the SD of
624 the filtered signal. As stated above, a circular distance threshold of 2.5 µm (AP-evoked activity
625 measurements) or 1000 µm (spontaneous activity measurements) around each event was
626 enforced to avoid unspecific detection of close by events in a single frame. When analyzing AP-
627 evoked activity measurements, we only considered events that were detected within 1 s of the
628 stimulus.

629 In order to generate activity maps as those shown in **Figure 2A**, we counted the number of
630 detected events in each ROI and overlaid an inverted and contrast-adjusted IHC image of the
631 respective protein at the NMJ with circles of corresponding sizes. The average signals shown in

632 **Figure. 1F** were generated by averaging all detected events in each cell, and then averaging over
633 all cell means.

634 **Spontaneous event detection between evoked events**

635 Besides the "sequential" way of analyzing spontaneous activity measurements and then evoked
636 activity measurements as described above, we also quantified spontaneous events that happened
637 between stimuli ("interleaved") as shown in **Figure 2 – figure supplement 3**. For this, we
638 altered the procedure described above by one detail. While everything else happened as in our
639 conventional approach to measure spontaneous activity, we suppressed the detection of evoked
640 events and instead quantified SV release between stimuli by creating an exclusion list. This list
641 included all time points 1000 ms after the stimulus, within which no fluorescence peaks would
642 be considered as a signal.

643 **Survival analysis**

644 A survival analysis quantifies the amount of "surviving" samples (in this case exclusively
645 spontaneously active AZs) in face of an event that "kills" those samples (in this case trying to
646 evoke release by a stimulus), i.e. switches them from one state to another over the course of the
647 treatment. To analyze how many spontaneously active ROIs would "survive", or maintain their
648 exclusively spontaneous state by not showing any AP-evoked activity in the AP-evoked activity
649 measurement (**Figure 2 – figure supplement 1**), we proceeded as follows. We loaded the results
650 from the analysis of spontaneous and AP-evoked activity measurements (described above)
651 containing all activity time points and AZ identities of spontaneous or evoked events into
652 MATLAB. We then first found the number and identity of all AZs showing spontaneous activity.
653 We created a data vector containing as many data points as there were frames in the AP-evoked
654 activity recording (3600 over 180 s) and filled all positions with the number of AZs showing

655 spontaneous activity we had found. Then, we found all time points of AP-evoked events in these
656 AZs and subtracted 1 from the previously created vector at the time points of the evoked event to
657 the end of the vector, resulting in a decreasing amount of exclusively spontaneously active AZs
658 over the time of the AP-evoked activity measurement. For each cell, we then set the initial
659 amount of exclusively spontaneously active AZs in that cell to 1 (100 %). Two models
660 describing the mono-exponential survival decay were compared using Akaike's information
661 criterion (AIC; Akaike, 1974) to verify our approach as shown in equations (3) and (4), either
662 excluding or including a plateau value of "surviving" exclusively spontaneously active AZs,
663 respectively.

664 *(3)* $surviving\ fraction(t) = exp^{-K*t}$

665 *(4)* $surviving\ fraction(t) = (1 - plateau) * exp^{-K*t} + plateau$

666 In equations (3) and (4), t is the timepoint at which survival is assessed, and K is the decay
667 constant related to survival "half-life" (the timepoint at which half of the non-surviving AZs will
668 have "died") as $t_{1/2} = \frac{\ln(2)}{K}$. The plateau value represents the fraction of AZs that will not "turn"
669 from spontaneous to mixed mode regardless of further stimulation. The difference in AIC
670 warranted the use of the more complex equation (4).

671 **Analysis of relation between AP-evoked and spontaneous events**

672 The response is number of evoked responses, which is analyzed with a generalized linear model
673 using a negative binomial response distribution with a log link. This is a distribution for counts
674 (a generalization of the Poisson distribution allowing for a flexible variance). The number of
675 evoked events is modelled as a function of spontaneous events with a random effect of animal on

676 the intercept (each animal has its own level). The number of spontaneous events enters as a
677 factor.

678 To test for an increasing monotonic trend in the four estimated values of the mean of evoked
679 events as a function of number of spontaneous events, we used the nonparametric Mann-Kendall
680 trend test against a positive trend in a time series (Mann, 1945). The null is that there is no trend,
681 so a small (one-sided) p-value suggests a positive monotonic trend. This is different from the test
682 of an effect, which simply tests if the 4 estimated mean values can be assumed to be equal. The
683 test was performed with the R-package trend, version 1.1.4, with option alternative = "greater"
684 (Thorsten Pohlert, 2016). R package version 1.1.4. https://CRAN.R-project.org/package=trend

685 **Automated spontaneous event detection**

686 For the automated detection of spontaneous vesicle fusion without respect to AZ positions shown
687 in **Figure 1 – figure supplement 1B-F,H** we developed an additional set of custom MATLAB
688 code. Single steps and results of the whole procedure on a single event are shown in **Figure 1 –**
689 **figure supplement 2**. Stabilized 8-bit grey scale multipage .TIF-video files (**Figure 1 – figure**
690 **supplement 2A**) were loaded into MATLAB, where the user could then manually select an area
691 of the video with the NMJ of interest. Using the MATLAB function *bwboundaries*, a logical
692 mask was then generated to find all pixels within the manually selected ROI. The chosen area
693 was then extended by 20 pixels to each side, generating a rectangular selection taken from the
694 original video. This cropped video was then further processed by slightly reducing noise using
695 the *medfilt3* function (**Figure 1 – figure supplement 2B**), which smoothes noise in 3D arrays by
696 taking the median grey value in a 3x3x3 pixel neighborhood. Next, the background was
697 subtracted to leave only transient increases in fluorescence. For this, a maximum projection of 10
698 closely preceding frames was generated for every frame of the video, which was then subtracted

699 from the current frame, where every resulting negative value was set to 0 (**Figure 1 – figure**
700 **supplement 2C**). To avoid removing parts of an event, a 'lag' of 5 frames was included before
701 the currently observed frame, resulting in a sequence of frames from the 15th to 6th before the
702 current frame for the background subtraction. Every iteration of this process resulted in a single
703 frame that was devoid of any basal GCaMP signal and excessive noise, only leaving transient
704 fluorescence peaks that deviated from the brightest features of the last 15th through 6th frames. In
705 addition to this background-subtracted video, another one was generated with the only difference
706 being that here, instead of the maximum projection or 10 frames, an average projection of the
707 same 10 frames was used to subtract the background. This video was then used for the exact
708 determination of events by a 2D-Gaussian fit as described further down. A Gaussian filter
709 (function *imgaussfilt* with a sigma of 3 pixels) was then applied to the resulting video for further
710 noise removal (**Figure 1 – figure supplement 2D**). This was necessary for the next step, in
711 which regions of connected (continuously bright) pixels above a threshold grey value of 2, and
712 within the manual selection, were identified (**Figure 1 – figure supplement 2E**). For each of the
713 identified regions, the median x,y-coordinates were found and temporarily defined as the
714 location of the event (**Figure 1 – figure supplement 2F**). Detected events within 10 pixels of the
715 edge of the video were removed, as they represented noise and were located outside the manual
716 NMJ selection. A square 39x39 pixel region was then chosen around each event and a Gaussian
717 fit was performed on a maximal projection of 6 frames (peak frame and 5 succeeding frames) of
718 the second background-subtracted video, where the average of the 15th to 6th preceding frame
719 was subtracted from each frame (**Figure 1 – figure supplement 2G**), as follows. A 2D-Gaussian
720 was simulated (the 'simulated image', **Figure 1 – figure supplement 2H**) and fit to a maximal
721 projection of six 39x39 px frames of an event (the 'temporary image') using equation (5):

722 (5) $\text{Gaussian}(x, y) = A * \exp^{-(\frac{(x-x_0)^2}{2*c^2}+\frac{(y-y_0)^2}{2*c^2})} + baseline$

723 (6) $FWHM = 2 * \sqrt{2 * \ln(2)} * c = 2.3548 * c$

724 In equation (5), *x* and *y* are any of the coordinates on the image of the current event, x_0 and y_0 are
725 the center coordinates of that image, *c* is a non-zero variable related to the full-width at half
726 maximum (FWHM) of the Gaussian function as shown in equation (6), and *baseline* is a
727 background correction factor. While the separation of x- and y-spread would allow non-
728 symmetrical Gaussian fits, these parameters were kept identical in the fit, making the spread of
729 the Gaussian uniform in 2D. An optimization procedure with the MATLAB function *fminsearch*
730 was used to find the best parameters for the center x,y-coordinate of the Gaussian, its amplitude,
731 its sigma value, and the baseline. An initial value of 20 was chosen for all five parameters. As a
732 measure of the quality of the fit, a cost function was used that calculated the difference between
733 the temporary image and the simulated image by subtracting them. As the success of *fminsearch*
734 depends, among other factors, on the initial parameters, the optimization was additionally
735 repeated three times with the best fit values of the previous run. The same optimization
736 procedure with a genetic algorithm (which is less biased regarding initial parameters) yielded the
737 same results at vastly longer processing times.

738 The analysis of spontaneous event amplitudes over increasing calcium concentrations shown in
739 **Figure 1 – figure supplement 1H** was performed in *Mhc-myrGCaMP5G/+* larvae with the
740 script described above at $[Ca^{2+}]_{ext.}$ of 0.4, 0.75, 1.5, 3, 6 and 12 mM in HL3 by exchanging the
741 external solutions between recordings in one animal and taking the cell-wise mean of GCaMP
742 signals at their peak. The nonlinear fit on the cell-wise means was performed by assuming a Hill-
743 relationship, where binding of Ca^{2+} to the sensor occurs with cooperativity *h*, and half-maximal

fluorescence is reached at a concentration of $[Ca^{2+}]_{ext.}$ of K_A as shown in equation (7). In that equation, F_{max} is the asymptotic maximal value of fluorescence at high $[Ca^{2+}]_{ext.}$, and C is a baseline correction to allow a baseline fluorescence different from 0.

$$(7)\ F([Ca^{2+}]_{ext}]) = F_{max} * \frac{[Ca^{2+}]_{ext}{}^{h}}{K_A{}^{h} + [Ca^{2+}]_{ext}{}^{h}} + C$$

Data and software availability

Source data is submitted for all figures. All ImageJ and MATLAB code used in this paper will be made available by the corresponding author (A.M.W., awalter@sund.ku.dk) upon reasonable request.

Author contributions (CRediT taxonomy)

Conceptualization, A.T.G. and A.M.W.; Formal Analysis, A.T.G., A.W.M., M.J. and T.W.B.G.; Funding Acquisition, A.M.W.; Investigation, A.T.G., A.W.M., M.J., S.D., A.M.W. and T.W.B.G; Software, A.T.G. and A.M.W.; Supervision, A.M.W.; Visualization, A.T.G., A.W.M., M.J. and T.W.B.G; Writing – Original Draft, A.T.G. and A.M.W. Corresponding & Lead Author, A.M.W. (awalter@sund.ku.dk)

Acknowledgments

We thank Stephan Sigrist and Volker Haucke for helpful discussion of the manuscript. We would like to thank Sabine Hahn for excellent technical assistance. M.J. was funded by a PhD-

763 fellowship from the Einstein Center for Neurosciences Berlin. This work was funded by grants
764 from the Deutsche Forschungsgemeinschaft (DFG, German Research Foundation): Project-
765 ID 278001972, TRR 186 to A.M.W. and Project-ID 261020751, Emmy-Noether Programme to
766 A.M.W.. This work was supported by the Novo Nordisk Foudation: Grant number:
767 NNF19OC0056047, Young Investigator Award to A.M.W..

768

769 **Competing Interests**

770 All authors confirm the absence of any financial or non-financial competing interests.

References

Akaike, H. (1974). A new look at the statistical model identification. IEEE Trans. Automat. Contr. *19*, 716–723.

Akbergenova, Y., Cunningham, K.L., Zhang, Y.V., Weiss, S., and Littleton, J.T. (2018). Characterization of developmental and molecular factors underlying release heterogeneity at Drosophila synapses. eLife *7*.

Andreae, L.C., Fredj, N.B., and Burrone, J. (2012). Independent vesicle pools underlie different modes of release during neuronal development. Journal of Neuroscience *32*, 1867–1874.

Atasoy, D., Ertunc, M., Moulder, K.L., Blackwell, J., Chung, C., Su, J., and Kavalali, E.T. (2008). Spontaneous and evoked glutamate release activates two populations of NMDA receptors with limited overlap. Journal of Neuroscience *28*, 10151–10166.

Bal, M., Leitz, J., Reese, A.L., Ramirez, D.M.O., Durakoglugil, M., Herz, J., Monteggia, L.M., and Kavalali, E.T. (2013). Reelin mobilizes a VAMP7-dependent synaptic vesicle pool and selectively augments spontaneous neurotransmission. Neuron *80*, 934–946.

Böhme, M.A., Beis, C., Reddy-Alla, S., Reynolds, E., Mampell, M.M., Grasskamp, A.T., Lützkendorf, J., Bergeron, D.D., Driller, J.H., Babikir, H., Göttfert, F., Robinson, I.M., O'Kane, C.J., Hell, S.W., Wahl, M.C., Stelzl, U., Loll, B., Walter, A.M., and Sigrist, S.J. (2016). Active zone scaffolds differentially accumulate Unc13 isoforms to tune Ca(2+) channel-vesicle coupling. Nature neuroscience *19*, 1311–1320.

Broadie, K., Bellen, H.J., DiAntonio, A., Littleton, J.T., and Schwarz, T.L. (1994). Absence of synaptotagmin disrupts excitation-secretion coupling during synaptic transmission. Proc Natl Acad Sci USA *91*, 10727–10731.

Broadie, K., Prokop, A., Bellen, H.J., O'Kane, C.J., Schulze, K.L., and Sweeney, S.T. (1995). Syntaxin and synaptobrevin function downstream of vesicle docking in drosophila. Neuron *15*, 663–673.

Brose, N., Rosenmund, C., and Rettig, J. (2000). Regulation of transmitter release by Unc-13 and its homologues. Current opinion in neurobiology *10*, 303–311.

Courtney, N.A., Briguglio, J.S., Bradberry, M.M., Greer, C., and Chapman, E.R. (2018). Excitatory and Inhibitory Neurons Utilize Different Ca2+ Sensors and Sources to Regulate Spontaneous Release. Neuron *98*, 977-991.e5.

Davis, G.W., and Müller, M. (2015). Homeostatic control of presynaptic neurotransmitter release. Annual review of physiology *77*, 251–270.

Deitcher, D.L., Ueda, A., Stewart, B.A., Burgess, R.W., Kidokoro, Y., and Schwarz, T.L. (1998). Distinct Requirements for Evoked and Spontaneous Release of Neurotransmitter Are Revealed by Mutations in the Drosophila Gene neuronal-synaptobrevin. Journal of Neuroscience *18*, 2028–2039.

Delvendahl, I., Kita, K., and Müller, M. (2019). Rapid and sustained homeostatic control of presynaptic exocytosis at a central synapse. Proc Natl Acad Sci USA *116*, 23783–23789.

Dittman, J.S. (2019). Unc13: a multifunctional synaptic marvel. Current opinion in neurobiology *57*, 17–25.

811 Ermolyuk, Y.S., Alder, F.G., Surges, R., Pavlov, I.Y., Timofeeva, Y., Kullmann, D.M., and
812 Volynski, K.E. (2013). Differential triggering of spontaneous glutamate release by P/Q-, N- and
813 R-type Ca2+ channels. Nature neuroscience *16*, 1754–1763.

814 Farsi, Z., Walde, M., Klementowicz, A.E., Paraskevopoulou, F., and Woehler, A. (2021). Single
815 synapse glutamate imaging reveals multiple levels of release mode regulation in mammalian
816 synapses. iScience *24*, 101909.

817 Fatt, P., and Katz, B. (1952). Spontaneous subthreshold activity at motor nerve endings. The
818 Journal of physiology *117*, 109–128.

819 Fouquet, W., Owald, D., Wichmann, C., Mertel, S., Depner, H., Dyba, M., Hallermann, S.,
820 Kittel, R.J., Eimer, S., and Sigrist, S.J. (2009). Maturation of active zone assembly by Drosophila
821 Bruchpilot. The Journal of cell biology *186*, 129–145.

822 Frank, C.A., Kennedy, M.J., Goold, C.P., Marek, K.W., and Davis, G.W. (2006). Mechanisms
823 underlying the rapid induction and sustained expression of synaptic homeostasis. Neuron *52*,
824 663–677.

825 Fredj, N.B., and Burrone, J. (2009). A resting pool of vesicles is responsible for spontaneous
826 vesicle fusion at the synapse. Nature neuroscience *12*, 751–758.

827 Geppert, M., Goda, Y., Hammer, R.E., Li, C., Rosahl, T.W., Stevens, C.F., and Südhof, T.C.
828 (1994). Synaptotagmin I: A major Ca2+ sensor for transmitter release at a central synapse. Cell
829 *79*, 717–727.

830 Goel, P., Li, X., and Dickman, D. (2017). Disparate Postsynaptic Induction Mechanisms
831 Ultimately Converge to Drive the Retrograde Enhancement of Presynaptic Efficacy. Cell reports
832 *21*, 2339–2347.

833 Goswami, S.P., Bucurenciu, I., and Jonas, P. (2012). Miniature IPSCs in hippocampal granule
834 cells are triggered by voltage-gated Ca2+ channels via microdomain coupling. Journal of
835 Neuroscience *32*, 14294–14304.

836 Graf, E.R., Daniels, R.W., Burgess, R.W., Schwarz, T.L., and DiAntonio, A. (2009). Rab3
837 dynamically controls protein composition at active zones. Neuron *64*, 663–677.

838 Groemer, T.W., and Klingauf, J. (2007). Synaptic vesicles recycling spontaneously and during
839 activity belong to the same vesicle pool. Nature neuroscience *10*, 145–147.

840 Groffen, A.J., Martens, S., Díez Arazola, R., Cornelisse, L.N., Lozovaya, N., Jong, A.P.H. de,
841 Goriounova, N.A., Habets, R.L.P., Takai, Y., Borst, J.G., Brose, N., McMahon, H.T., and
842 Verhage, M. (2010). Doc2b is a high-affinity Ca2+ sensor for spontaneous neurotransmitter
843 release. Science (New York, N.Y.) *327*, 1614–1618.

844 Harris, K.P., and Littleton, J.T. (2015). Transmission, Development, and Plasticity of Synapses.
845 Genetics *201*, 345–375.

846 Held, R.G., and Kaeser, P.S. (2018). ELKS active zone proteins as multitasking scaffolds for
847 secretion. Open biology *8*.

848 Hou, J., Tamura, T., and Kidokoro, Y. (2008). Delayed synaptic transmission in Drosophila
849 cacophonynull embryos. Journal of neurophysiology *100*, 2833–2842.

850 Hua, Y., Sinha, R., Martineau, M., Kahms, M., and Klingauf, J. (2010). A common origin of
851 synaptic vesicles undergoing evoked and spontaneous fusion. Nature neuroscience *13*, 1451–
852 1453.

853 Huntwork, S., and Littleton, J.T. (2007). A complexin fusion clamp regulates spontaneous
854 neurotransmitter release and synaptic growth. Nature neuroscience *10*, 1235–1237.

855 Jahn, R., and Fasshauer, D. (2012). Molecular machines governing exocytosis of synaptic
856 vesicles. Nature *490*, 201–207.

857 Kaeser, P.S., and Regehr, W.G. (2014). Molecular mechanisms for synchronous, asynchronous,
858 and spontaneous neurotransmitter release. Annual review of physiology *76*, 333–363.

859 Kavalali, E.T. (2015). The mechanisms and functions of spontaneous neurotransmitter release.
860 Nature reviews. Neuroscience *16*, 5–16.

861 Kittel, R.J., Wichmann, C., Rasse, T.M., Fouquet, W., Schmidt, M., Schmid, A., Wagh, D.A.,
862 Pawlu, C., Kellner, R.R., Willig, K.I., Hell, S.W., Buchner, E., Heckmann, M., and Sigrist, S.J.
863 (2006). Bruchpilot promotes active zone assembly, Ca2+ channel clustering, and vesicle release.
864 Science (New York, N.Y.) *312*, 1051–1054.

865 Kobbersmed, J.R.L., Grasskamp, A.T., Jusyte, M., Böhme, M.A., Ditlevsen, S., Sørensen, J.B.,
866 and Walter, A.M. (2020). Rapid regulation of vesicle priming explains synaptic facilitation
867 despite heterogeneous vesicle:Ca2+ channel distances. eLife *9*.

868 Kochubey, O., Lou, X., and Schneggenburger, R. (2011). Regulation of transmitter release by
869 Ca(2+) and synaptotagmin: insights from a large CNS synapse. Trends in Neurosciences *34*,
870 237–246.

871 Koenig, J.H., and Ikeda, K. (1999). Contribution of active zone subpopulation of vesicles to
872 evoked and spontaneous release. Journal of neurophysiology *81*, 1495–1505.

873 Littleton, J.T., and Bellen, H.J. (1995). Synaptotagmin controls and modulates synaptic-vesicle
874 fusion in a Ca2+-dependent manner. Trends in Neurosciences *18*, 177–183.

875 Littleton, J.T., Stern, M., Schulze, K., Perin, M., and Bellen, H.J. (1993). Mutational analysis of
876 Drosophila synaptotagmin demonstrates its essential role in Ca2+-activated neurotransmitter
877 release. Cell *74*, 1125–1134.

878 Mann, H.B. (1945). Nonparametric Tests Against Trend. Econometrica *13*, 245.

879 Martin, J.A., Hu, Z., Fenz, K.M., Fernandez, J., and Dittman, J.S. (2011). Complexin has
880 opposite effects on two modes of synaptic vesicle fusion. Current Biology *21*, 97–105.

881 Melom, J.E., Akbergenova, Y., Gavornik, J.P., and Littleton, J.T. (2013). Spontaneous and
882 evoked release are independently regulated at individual active zones. Journal of Neuroscience
883 *33*, 17253–17263.

884 Miki, T., Malagon, G., Pulido, C., Llano, I., Neher, E., and Marty, A. (2016). Actin- and Myosin-
885 Dependent Vesicle Loading of Presynaptic Docking Sites Prior to Exocytosis. Neuron *91*, 808–
886 823.

887 Muhammad, K., Reddy-Alla, S., Driller, J.H., Schreiner, D., Rey, U., Böhme, M.A., Hollmann,
888 C., Ramesh, N., Depner, H., Lützkendorf, J., Matkovic, T., Götz, T., Bergeron, D.D.,
889 Schmoranzer, J., Goettfert, F., Holt, M., Wahl, M.C., Hell, S.W., Scheiffele, P., Walter, A.M.,

890 Loll, B., and Sigrist, S.J. (2015). Presynaptic spinophilin tunes neurexin signalling to control
891 active zone architecture and function. Nat Commun *6*, 8362.

892 Peled, E.S., and Isacoff, E.Y. (2011). Optical quantal analysis of synaptic transmission in wild-
893 type and rab3-mutant Drosophila motor axons. Nature neuroscience *14*, 519–526.

894 Peled, E.S., Newman, Z.L., and Isacoff, E.Y. (2014). Evoked and spontaneous transmission
895 favored by distinct sets of synapses. Current Biology *24*, 484–493.

896 Qin, G., Schwarz, T., Kittel, R.J., Schmid, A., Rasse, T.M., Kappei, D., Ponimaskin, E.,
897 Heckmann, M., and Sigrist, S.J. (2005). Four different subunits are essential for expressing the
898 synaptic glutamate receptor at neuromuscular junctions of Drosophila. Journal of Neuroscience
899 *25*, 3209–3218.

900 Ramirez, D.M.O., Khvotchev, M., Trauterman, B., and Kavalali, E.T. (2012). Vti1a identifies a
901 vesicle pool that preferentially recycles at rest and maintains spontaneous neurotransmission.
902 Neuron *73*, 121–134.

903 Reddy-Alla, S., Böhme, M.A., Reynolds, E., Beis, C., Grasskamp, A.T., Mampell, M.M.,
904 Maglione, M., Jusyte, M., Rey, U., Babikir, H., McCarthy, A.W., Quentin, C., Matkovic, T.,
905 Bergeron, D.D., Mushtaq, Z., Göttfert, F., Owald, D., Mielke, T., Hell, S.W., Sigrist, S.J., and
906 Walter, A.M. (2017). Stable Positioning of Unc13 Restricts Synaptic Vesicle Fusion to Defined
907 Release Sites to Promote Synchronous Neurotransmission. Neuron *95*, 1350-1364.e12.

908 Reese, A.L., and Kavalali, E.T. (2016). Single synapse evaluation of the postsynaptic NMDA
909 receptors targeted by evoked and spontaneous neurotransmission. eLife *5*.

910 Reim, K., Mansour, M., Varoqueaux, F., McMahon, H.T., Südhof, T.C., Brose, N., and
911 Rosenmund, C. (2001). Complexins Regulate a Late Step in Ca2+-Dependent Neurotransmitter
912 Release. Cell *104*, 71–81.

913 Richmond, J.E., and Broadie, K.S. (2002). The synaptic vesicle cycle: exocytosis and
914 endocytosis in Drosophila and C. elegans. Current opinion in neurobiology *12*, 499–507.

915 Rizo, J. (2018). Mechanism of neurotransmitter release coming into focus. Protein science : a
916 publication of the Protein Society *27*, 1364–1391.

917 Ryglewski, S., Lance, K., Levine, R.B., and Duch, C. (2012). Ca(v)2 channels mediate low and
918 high voltage-activated calcium currents in Drosophila motoneurons. The Journal of physiology
919 *590*, 809–825.

920 Sakamoto, H., Ariyoshi, T., Kimpara, N., Sugao, K., Taiko, I., Takikawa, K., Asanuma, D.,
921 Namiki, S., and Hirose, K. (2018). Synaptic weight set by Munc13-1 supramolecular assemblies.
922 Nature neuroscience *21*, 41–49.

923 Sara, Y., Bal, M., Adachi, M., Monteggia, L.M., and Kavalali, E.T. (2011). Use-dependent
924 AMPA receptor block reveals segregation of spontaneous and evoked glutamatergic
925 neurotransmission. Journal of Neuroscience *31*, 5378–5382.

926 Sara, Y., Virmani, T., Deák, F., Liu, X., and Kavalali, E.T. (2005). An isolated pool of vesicles
927 recycles at rest and drives spontaneous neurotransmission. Neuron *45*, 563–573.

928 Schneggenburger, R., and Rosenmund, C. (2015). Molecular mechanisms governing Ca(2+)
929 regulation of evoked and spontaneous release. Nature neuroscience *18*, 935–941.

930 Schoch, S., Deák, F., Königstorfer, A., Mozhayeva, M., Sara, Y., Südhof, T.C., and Kavalali,
931 E.T. (2001). SNARE function analyzed in synaptobrevin/VAMP knockout mice. Science (New
932 York, N.Y.) *294*, 1117–1122.

933 Shahrezaei, V., Cao, A., and Delaney, K.R. (2006). Ca2+ from one or two channels controls
934 fusion of a single vesicle at the frog neuromuscular junction. Journal of Neuroscience *26*, 13240–
935 13249.

936 Sigrist, S.J., Reiff, D.F., Thiel, P.R., Steinert, J.R., and Schuster, C.M. (2003). Experience-
937 dependent strengthening of Drosophila neuromuscular junctions. Journal of Neuroscience *23*,
938 6546–6556.

939 Stewart, B., Atwood, H.L., Renger, J.J., Wang, J., and Wu, C.F. (1994). Improved stability of
940 Drosophila larval neuromuscular preparations in haemolymph-like physiological solutions.
941 Journal of comparative physiology. A, Sensory, neural, and behavioral physiology *175*, 179–191.

942 Südhof, T.C. (2012a). Calcium control of neurotransmitter release. Cold Spring Harbor
943 perspectives in biology *4*, a011353.

944 Südhof, T.C. (2012b). The presynaptic active zone. Neuron *75*, 11–25.

945 Südhof, T.C. (2013). Neurotransmitter release: the last millisecond in the life of a synaptic
946 vesicle. Neuron *80*, 675–690.

947 Südhof, T.C., and Rothman, J.E. (2009). Membrane fusion: grappling with SNARE and SM
948 proteins. Science (New York, N.Y.) *323*, 474–477.

949 Tang, A.-H., Chen, H., Li, T.P., Metzbower, S.R., MacGillavry, H.D., and Blanpied, T.A.
950 (2016). A trans-synaptic nanocolumn aligns neurotransmitter release to receptors. Nature *536*,
951 210–214.

952 Thévenaz, P., Ruttimann, U.E., and Unser, M. (1998). A pyramid approach to subpixel
953 registration based on intensity. IEEE transactions on image processing : a publication of the
954 IEEE Signal Processing Society *7*, 27–41.

955 Thorsten Pohlert (2016). Non-parametric trend tests and change-point detection. CC BY-ND, 4.

956 Toonen, R.F.G., and Verhage, M. (2007). Munc18-1 in secretion: lonely Munc joins SNARE
957 team and takes control. Trends in Neurosciences *30*, 564–572.

958 Truckenbrodt, S., and Rizzoli, S.O. (2014). Spontaneous vesicle recycling in the synaptic bouton.
959 Frontiers in cellular neuroscience *8*, 409.

960 Ullrich, A., Böhme, M.A., Schöneberg, J., Depner, H., Sigrist, S.J., and Noé, F. (2015).
961 Dynamical Organization of Syntaxin-1A at the Presynaptic Active Zone. PLoS computational
962 biology *11*, e1004407.

963 Walter, A.M., Böhme, M.A., and Sigrist, S.J. (2018). Vesicle release site organization at synaptic
964 active zones. Neuroscience research *127*, 3–13.

965 Walter, A.M., Haucke, V., and Sigrist, S.J. (2014). Neurotransmission: spontaneous and evoked
966 release filing for divorce. Current Biology *24*, R192-4.

967 Weber, J.P., Reim, K., and Sørensen, J.B. (2010). Opposing functions of two sub-domains of the
968 SNARE-complex in neurotransmission. The EMBO journal *29*, 2477–2490.

969 Wilhelm, B.G., Groemer, T.W., and Rizzoli, S.O. (2010). The same synaptic vesicles drive
970 active and spontaneous release. Nature neuroscience *13*, 1454–1456.

971 Xu, J., Pang, Z.P., Shin, O.-H., and Südhof, T.C. (2009). Synaptotagmin-1 functions as a Ca2+
972 sensor for spontaneous release. Nature neuroscience *12*, 759–766.

973 Yang, X., Cao, P., and Südhof, T.C. (2013). Deconstructing complexin function in activating and
974 clamping Ca2+-triggered exocytosis by comparing knockout and knockdown phenotypes. Proc
975 Natl Acad Sci USA *110*, 20777–20782.

976 Zefirov, A., Benish, T., Fatkullin, N., Cheranov, S., and Khazipov, R. (1995). Localization of
977 active zones. Nature *376*, 393–394.

978 Zhang, B., and Stewart, B. (2010). Electrophysiological recording from Drosophila larval body-
979 wall muscles. Cold Spring Harbor protocols *2010*, pdb.prot5487.

980